

UC Berkeley

UC Berkeley Previously Published Works

Title

Structure of the C9orf72 ARF GAP complex that is haploinsufficient in ALS and FTD

Permalink

<https://escholarship.org/uc/item/7951x4cx>

Journal

Nature, 585(7824)

ISSN

0028-0836

Authors

Su, Ming-Yuan

Fromm, Simon A

Zoneu, Roberto

et al.

Publication Date

2020-09-10

DOI

10.1038/s41586-020-2633-x

Peer reviewed

1 **Structure of the lysosomal SCARF (L-SCARF) complex, an Arf GAP**
2 **haploinsufficient in ALS and FTD**

3

4 **Authors:** Ming-Yuan Su¹, Roberto Zoncu¹ and James H. Hurley¹,

5

6 **Affiliations:** ¹Department of Molecular and Cell Biology and California Institute for
7 Quantitative Biosciences, University of California, Berkeley, Berkeley, CA 94720

8

9

10 **Abstract**

11 Mutation of *C9ORF72* is the most prevalent defect in amyotrophic lateral sclerosis
12 (ALS) and frontal temporal degeneration (FTD). Together with hexanucleotide repeat
13 expansion, haploinsufficiency of *C9ORF72* contributes to neuronal dysfunction. We
14 determined the structure of the SMCR8-C9orf72-WDR41 complex by cryo-EM.
15 C9orf72 and SMCR8 are both longin-DENN domain proteins, while WDR41 is a
16 beta-propeller protein that binds to SMCR8 such that the whole structure resembles
17 an eye slip hook. Contacts between WDR41 and SMCR8^{DENN} drive lysosomal
18 localization in amino acid starvation. The structure suggested that SMCR8-C9orf72
19 was a small GTPase activating protein (GAP). We found that
20 SMCR8-C9orf72-WDR41 is a GAP for Arf family small GTPases, and refer to it as
21 the Lysosomal SMCR8-C9orf72 Arf GAP ("L-SCARF") complex. These data
22 rationalize the function of C9orf72 both in normal physiology and in ALS/FTD.

23

24

25

26

27

28 **Main**

29 Expansion of hexanucleotide GGGGCC repeats in the first intron of *C9ORF72* is the
30 most prevalent genetic cause of amyotrophic lateral sclerosis (ALS) and frontal
31 temporal degeneration (FTD) in humans^{1,2}, accounting for approximately 40% of
32 familial ALS, 5% of sporadic ALS and 10-50 % of FTD³. Two hypotheses, not
33 mutually exclusive, have been put forward to explain how the mutation leads to
34 progressive loss of neurons. The toxic gain of function hypothesis suggests that toxic
35 molecules, including RNA and dipeptide repeat aggregates, disrupt neural function
36 and lead to their destruction⁴⁻¹⁴. The loss of function hypothesis is based on the
37 observation of a reduction in C9orf72 mRNA and protein levels in patients. In
38 powerful support of the latter, the endogenous function of C9orf72 is essential for
39 microglia¹⁵ and for normal axonal actin dynamics in motor neurons¹⁶, and restoring
40 normal C9orf72 protein expression rescues function in *c9orf72* model neurons¹⁷.

41 C9orf72 is a longin and DENN (differentially expressed in normal and neoplastic
42 cells) domain-containing protein¹⁸ (Fig. 1a). C9orf72 exists in cells as stable complex
43 with another longin and DENN-containing protein, Smith-Magenis syndrome
44 chromosome region, candidate 8 (SMCR8), and the WD repeat-containing protein 41
45 (WDR41)¹⁹⁻²⁴ (Fig. 1a). For reasons described below, we will refer to
46 SMCR8-C9orf72 as the "SCARF" complex. The main role of WDR41 appears to be
47 to target SCARF to lysosomes²⁵ via an interaction with the transporter PQ loop
48 repeat-containing 2 (PQLC2)²⁶. We therefore refer to SMCR8-C9orf72-WDR41 as
49 the "L-SCARF" complex. Various cellular functions of SCARF in normal physiology
50 have been proposed, including regulation of Rab-positive endosomes²⁷, regulation of
51 Rab8a and Rab39b in membrane transport^{19,23}, regulation of the ULK1 complex in
52 autophagy^{20,23,24,28}, and regulation of mTORC1 at lysosomes^{21,22,29}. Thus far it has
53 been difficult to deconvolute which of these roles are direct *vs.* indirect. In order to
54 gain more insight, we reconstituted and purified the complex, determined its structure,
55 and assessed its function as a purified complex.

56 Full length human SCARF and L-SCARF were generated in HEK293 Gn-Ti
57 cells by simultaneous transient transfection of all subunits, and purified (Extended
58 Data Fig. 1). The structure of L-SCARF was determined at a resolution of 3.8 Å by
59 cryo-electron microscopy (cryo-EM) (Fig. 1b-c, Extended Data Fig. 2-4, Table 1). We
60 were able to visualize the ordered ~120 kDa portion of the complex, corresponding to
61 about 60 % of the total mass of the complex. The structure has the shape of an eye
62 slip hook with a long dimension of ~140 Å (Fig. 1c). The ring of the hook was
63 straightforward to assign to WDR41 by its appearance as an eight-bladed propeller.
64 The remainder of the density evidenced two longin domains at the tip of the hook,
65 with the bulk of the hook made up of two DENN domains. The SMCR8^{DENN} domain

66 is in direct contact with WDR41, whilst C9orf72 has no direct contact with WDR41.
67 The hook tip portion of the SMCR8^{longin} domain was assigned to residues S159-T210,
68 which were predicted to comprise a long helical extension unique to SMCR8^{longin}.
69 SMCR8^{longin} and SMCR8^{DENN} are near each other but not in direct contact, and are
70 connected by a helical linker consisting of residues T321-K363. Both domains of
71 C9orf72 are positioned between SMCR8^{longin} and SMCR8^{DENN}. This linear
72 arrangement of domains gives the overall complex an elongated shape.

73 To map WDR41 interactions and facilitate interpretation of the cryo-EM
74 structure, SCARF and L-SCARF complexes were subjected to hydrogen deuterium
75 exchange mass spectrometry (HDX-MS) for 0.5, 5, 50, 500 and 50,000 sec and
76 compared to each other (Fig. 2, Extended Data Fig. 1, 5, 6, Dataset 1). Excellent
77 peptide coverage (89, 87 and 80 % for SMCR8, C9orf72 and WDR41, respectively)
78 was achieved and consistent patterns were observed at all experimental time points.
79 Several regions in SMCR8 including the N-terminal 54 residues, residues V104-V118,
80 E212-I230, P257-F315, V378-I714 and V788-Y806 showed more than 50 %
81 deuterium uptake at 0.5 sec, indicating these regions are intrinsically disordered
82 regions (IDRs), consistent with sequence-based predictions. Nearly all of C9orf72
83 was protected from exchange, except for the N-terminal 21 residues and the
84 C-terminus. For WDR41, the N-terminal 24 residues, and the loops connecting blade
85 II-III (R128-C131), blade V-VI (R260-D270, L277-I284), internal loop of blade VII
86 and the loop connecting to VIII (R352-L357, M369-E396) were flexible.

87 Difference heat maps for C9orf72 and SMCR8 (Fig. 2a-b) showed that in
88 presence of WDR41, regions of the SMCR8^{DENN} including K363-L372 (SMCR8^{M1}),
89 P763-Q770 (SMCR8^{M2}), S729-V735 (SMCR8^{M3}), T807-D811 (SMCR8^{M4}) and
90 C-terminal K910-Y935 (SMCR8^{M5}) were protected from exchange (Fig. 2, Extended
91 Data Fig. 5, 6), consistent with the structure. There was no significant change in
92 C9orf72, with the exception of K388-R394 (C9orf72^{M1}) (Fig. 2). Regions showing
93 protection changes were mutagenized and tested in pull down experiments (Fig. 2c-d).
94 Except for the helical linker mutant SMCR8^{M1}, the mutations including SMCR8^{M2-M5}
95 abolished the interaction with WDR41. When WDR41 failed to pull down SMCR8
96 mutants, wild-type C9orf72 was not detected either. This confirms the structural
97 finding that SMCR8 bridges the other two components. Because C9orf72^{M1} retained
98 interaction with SMCR8-WDR41, we concluded that this region was protected by a
99 conformational change induced upon WDR41 binding, consistent with the lack of
100 direct interaction in the cryo-EM structure. The cryo-EM structure showed that
101 SMCR8 bound to blades VIII and C terminal helix of WDR41 (Fig. 3a-b). The pull
102 down experiment showed that the N-terminal residues E35-K40 of blade VIII and the
103 C-terminal helix S442-V459 are required for SMCR8 binding (Extended Data Fig.7).

104 Collectively, the HDX-MS and mutational results corroborate the structural
105 interpretation.

106 WDR41 is responsible for the reversible targeting of SCARF to lysosomes in
107 nutrient depletion²⁵. WDR41 in turns binds to lysosomes via PQLC2²⁶. We
108 co-transfected DNA encoding GFP-SMCR8, C9orf72, WDR41 and PQLC2-mRFP in
109 HEK293A cells. SMCR8 clustered on PQLC2-positive lysosomes in amino acid
110 depletion and was diffusely localized in the cytosol upon refeeding (Fig. 3c),
111 consistent with these reports^{25,26}. SMCR8 mutants deficient in WDR41 binding *in*
112 *vitro* did not colocalize with PQLC2-positive lysosomes, but rather were diffusely
113 localized in the cytosol even under amino acid-starved conditions (Fig. 3c-d). These
114 findings confirm that the WDR41 binding site on SMCR8 as mapped by cryo-EM and
115 HDX-MS is responsible for the lysosomal localization of the complex in amino-acid
116 starvation.

117 The structure showed that SMCR8^{longin} forms a heterodimer with C9orf72^{longin} in
118 the same manner as Nprl2-Nprl3 of the GATOR1 complex³⁰ and FLCN-FNIP2 in the
119 Lysosomal Folliculin Complex (LFC)^{31,32}. The Nprl2 and FLCN subunits of these
120 complexes are the GTPase activating proteins (GAPs) for the lysosomal small
121 GTPases RagA³³ and RagC³⁴, respectively. Structure-based alignment of SMCR8
122 with FLCN and Nprl2 showed they shared a conserved Arg finger residue^{31,32,35} (Fig.
123 4a), corresponding to SMCR8 Arg147. This Arg residue is exposed on the protein
124 surface near the center of a large concave surface that appears suitable for binding a
125 small GTPase (Extended Data Fig.8). Using a Trp fluorescence-based assay, we
126 assayed SCARF for GAP activity with respect to RagA or RagC and found none
127 detectable (Extended Data Fig. 9). We also assayed for GAP activity with respect to
128 Rab1a²⁸ and the late endosomal Rab7²⁷, and again, activity was undetectable
129 (Extended Data Fig. 9,10).

130 It has been reported that C9orf72 interacts with the small GTPases Arf1 and
131 Arf6³⁶ in neurons¹⁶, although the nature of the interaction is unknown. We found that
132 L-SCARF was an efficient GAP for Arf1 on the basis of both Trp fluorescence and
133 HPLC-based assays (Fig. 4). The Arf1^{Q71L} GTP locked mutant had no activity
134 (Fig.4b-c), nor did the version of the complex containing the SMCR8^{R147A} finger
135 mutation. FLCN-FNIP2 and GATOR1 had no GAP activity towards Arf1. SCARF
136 was as active as L-SCARF, consistent with the location of WDR41 on the opposite
137 side of the complex from Arg147. L-SCARF has activity against the other Arf
138 family members, Arf5 and Arf6, but not against the lysosomal Arf-like proteins Arl8a
139 and Arl8b (Extended Data Fig. 9, 10). These observations clarify the nature of the
140 reported C9orf72-Arf interaction by showing that the role of C9orf72 is to stabilize a
141 complex with SMCR8, which is in turn an efficient and selective GAP for Arf

142 GTPases. For this reason, we have adopted the term SCARF for SMCR8-C9orf72
143 ARF GAP for the complex, and L-SCARF for the WDR41-containing version that is
144 lysosomally localized in amino acid starvation.

145 These structural and functional data shed light on the normal function of C9orf72,
146 which is thought to contribute to neuronal loss of function in ALS and FTD¹⁷. The
147 structure shows that C9orf72 is the central component of its complex with SMCR8.
148 The longin and DENN domains of SMCR8 flank and are stabilized by C9orf72.
149 SMCR8 contains the binding site for WDR41 that is responsible for lysosomal
150 localization during amino acid starvation. The structure shows that SCARF belongs to
151 the same class of double-longin domain GAP complexes as GATOR1³⁰ and
152 FLCN-FNIP^{31,32}. Unlike GATOR1 and FLCN-FNIP, SCARF is inactive against Rag
153 GTPases, but is active against Arf GTPases instead. The GAP active site is located at
154 the opposite end of the complex from the lysosomal targeting site on WDR41.

155 A remaining question concerns the regulation of the Arf-GAP function of
156 SMCR8-C9orf72 in cells. Our *in vitro* observation that SCARF and L-SCARF have
157 comparable GAP activities suggests that, in cells, SMCR8-C9orf72 may regulate Arf
158 GTPases both in full nutrient conditions, when the complex is primarily localized in
159 the cytosol, and under amino acid starvation, when it relocates to the lysosomal
160 membrane via WDR41-PQLC2 interaction. However, additional factors could limit or
161 augment the Arf-GAP activity in either condition and restrict or enhance access to the
162 GTP-bound Arf substrate. Arf proteins are not observed on lysosomes, and their
163 closest lysosomal cousins, Arl8a and Arl8b, are not substrates for SCARF. Thus,
164 sequestration of L-SCARF on lysosomes could prevent it from regulating the Arfs in
165 *cis* under unfavorable metabolic conditions. Alternatively, L-SCARF could act in
166 *trans* on Arf bound to the membrane of a compartment other than the lysosome. Arf
167 GTPases are found on the Golgi, endosomes, plasma membrane, cytoskeleton, and in
168 the cytosol³⁶, and typically function on membranes in their active GTP-bound form.
169 Several reports have found C9orf72 to be associated with endosomes^{17,27,37} and the
170 cytoskeleton¹⁶, which are good candidates for the locus of the Arf substrate of
171 SCARF. The potential *trans* GAP activity of L-SCARF *vs.* endosomal or cytoskeletal
172 Arf would be facilitated by its elongated structure and the distal positioning of the
173 GAP and lysosomal localization sites (Fig. 4d).

174 The structure of the complex places it in the same class of heterodimeric
175 longin-DENN domain protein GAP complexes as FLCN-FNIP^{31,32}. FLCN-FNIP is a
176 major node for communicating lysosomal nutrient status to the nucleus by virtue of its
177 regulation of the RagC GTPase³⁴ and the phosphorylation of transcription factors
178 regulating lysosome biogenesis and autophagy³¹. These data show how C9orf72 is
179 stabilized on the lysosome in amino acid starvation by bridging contacts made by

180 SMCR8 to WDR41. They show that C9orf72 serves as the central hub that stabilizes
181 the SCARF complex, in which SMCR8 is the "business end" with respect to Arf GAP
182 activity. A number of physiological functions have been imputed to C9orf72 based on
183 protein interactions mapped in cells and in lysates, but it has been unclear what
184 biochemical activities belong to C9orf72 itself, as opposed to downstream and
185 indirect effects. Here, we established a direct function for purified SMCR8-C9orf72,
186 which we designate the SCARF complex for its robust and specific GAP activity on
187 Arf proteins. We found that this activity is comparable to that of other
188 well-established GAP complexes such as GATOR1 and FLCN-FNIP with respect to
189 their substrates. This activity likely explains how C9orf72 modulates actin dynamics
190 in neurons¹⁶. It has been reported that Arf1 promotes mTORC1 activation³⁸, so the
191 Arf GAP function of SCARF could explain how this complex antagonizes mTORC1²⁹.
192 Finally, multiple reports connect C9orf72 to endosomal sorting^{17,27,37}, a process in
193 which the role of Arfs is well-established³⁶. The structural and *in vitro* biochemical
194 data reported here thus provide a framework and a foothold for understanding how the
195 normal functions of C9orf72 relate to lysosomal signaling, autophagy, and neuronal
196 survival.

197

198

199

200

201

202

203

204

205

206

207

208

209

210

211

212

213

214

215

216

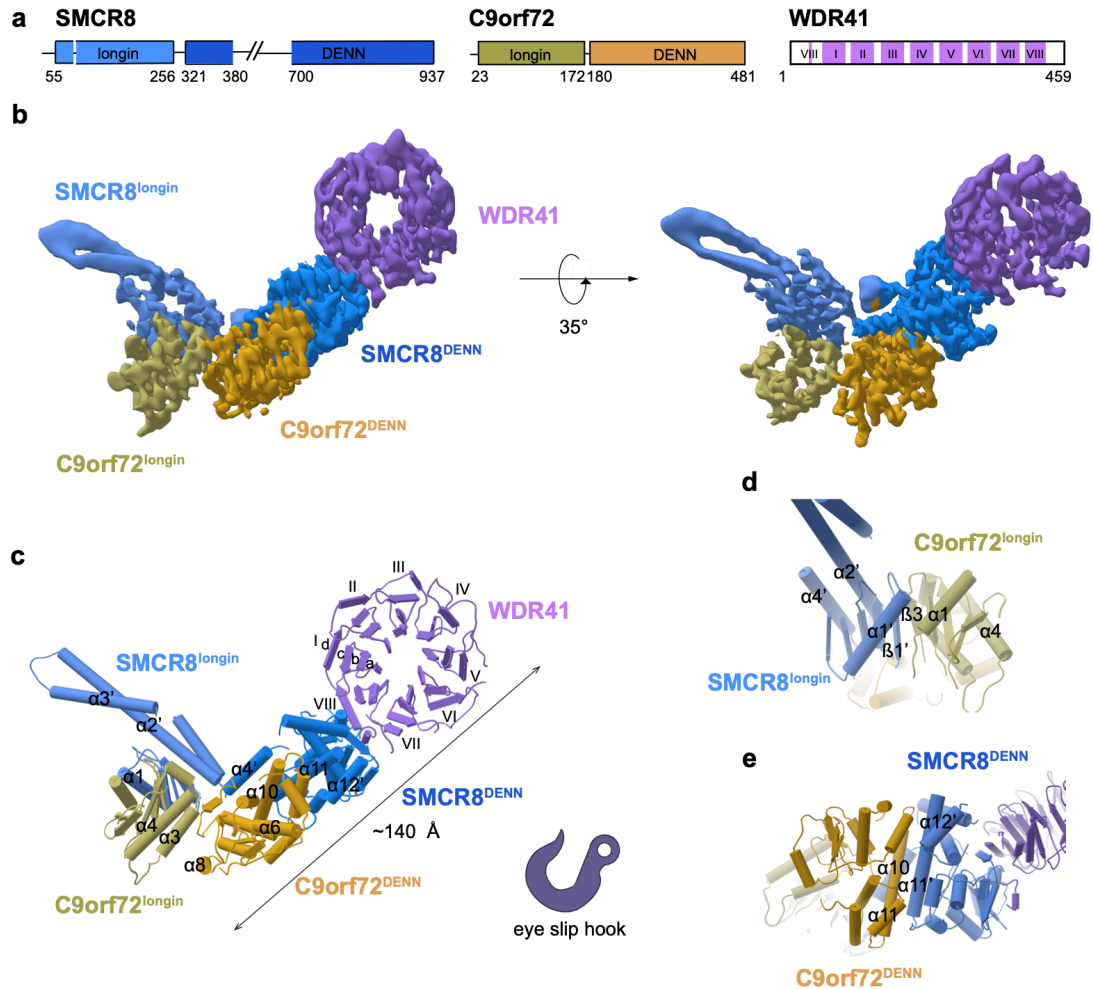
217

218 References

- 219 1 DeJesus-Hernandez, M. *et al.* Expanded GGGGCC hexanucleotide repeat in
220 noncoding region of C9ORF72 causes chromosome 9p-linked FTD and ALS.
221 *Neuron* 72, 245-256 (2011).
- 222 2 Renton, A. E. *et al.* A hexanucleotide repeat expansion in C9ORF72 is the
223 cause of chromosome 9p21-linked ALS-FTD. *Neuron* 72, 257-268 (2011).
- 224 3 Majounie, E. *et al.* Frequency of the C9orf72 hexanucleotide repeat expansion
225 in patients with amyotrophic lateral sclerosis and frontotemporal dementia: a
226 cross-sectional study. *Lancet Neurol* 11, 323-330 (2012).
- 227 4 Zhang, Y. J. *et al.* Heterochromatin anomalies and double-stranded RNA
228 accumulation underlie C9orf72 poly(PR) toxicity. *Science* 363 (2019).
- 229 5 Guo, Q. *et al.* In Situ Structure of Neuronal C9orf72 Poly-GA Aggregates
230 Reveals Proteasome Recruitment. *Cell* 172, 696-705 e612 (2018).
- 231 6 Lin, Y. *et al.* Toxic PR Poly-Dipeptides Encoded by the C9orf72 Repeat
232 Expansion Target LC Domain Polymers. *Cell* 167, 789-802 e712 (2016).
- 233 7 Lee, K. H. *et al.* C9orf72 Dipeptide Repeats Impair the Assembly, Dynamics,
234 and Function of Membrane-Less Organelles. *Cell* 167, 774-788 e717 (2016).
- 235 8 Zhang, K. *et al.* The C9orf72 repeat expansion disrupts nucleocytoplasmic
236 transport. *Nature* 525, 56-61 (2015).
- 237 9 Freibaum, B. D. *et al.* GGGGCC repeat expansion in C9orf72 compromises
238 nucleocytoplasmic transport. *Nature* 525, 129-133 (2015).
- 239 10 Chew, J. *et al.* Neurodegeneration. C9ORF72 repeat expansions in mice cause
240 TDP-43 pathology, neuronal loss, and behavioral deficits. *Science* 348,
241 1151-1154 (2015).
- 242 11 Mizielinska, S. *et al.* C9orf72 repeat expansions cause neurodegeneration in
243 *Drosophila* through arginine-rich proteins. *Science* 345, 1192-1194 (2014).
- 244 12 Kwon, I. *et al.* Poly-dipeptides encoded by the C9orf72 repeats bind nucleoli,
245 impede RNA biogenesis, and kill cells. *Science* 345, 1139-1145 (2014).
- 246 13 Haeusler, A. R. *et al.* C9orf72 nucleotide repeat structures initiate molecular
247 cascades of disease. *Nature* 507, 195-200 (2014).
- 248 14 Mori, K. *et al.* The C9orf72 GGGGCC repeat is translated into aggregating
249 dipeptide-repeat proteins in FTL/ALS. *Science* 339, 1335-1338 (2013).
- 250 15 O'Rourke, J. G. *et al.* C9orf72 is required for proper macrophage and
251 microglial function in mice. *Science* 351, 1324-1329 (2016).
- 252 16 Sivadasan, R. *et al.* C9ORF72 interaction with cofilin modulates actin
253 dynamics in motor neurons. *Nat Neurosci* 19, 1610-1618 (2016).
- 254 17 Shi, Y. *et al.* Haploinsufficiency leads to neurodegeneration in C9ORF72
255 ALS/FTD human induced motor neurons. *Nat Med* 24, 313-325 (2018).

- 256 18 Zhang, D., Iyer, L. M., He, F. & Aravind, L. Discovery of Novel DENN
257 Proteins: Implications for the Evolution of Eukaryotic Intracellular Membrane
258 Structures and Human Disease. *Frontiers in genetics* 3, 283 (2012).
- 259 19 Sellier, C. *et al.* Loss of C9ORF72 impairs autophagy and synergizes with
260 polyQ Ataxin-2 to induce motor neuron dysfunction and cell death. *EMBO J.*
261 35, 1276-1297 (2016).
- 262 20 Sullivan, P. M. *et al.* The ALS/FTLD associated protein C9orf72 associates
263 with SMCR8 and WDR41 to regulate the autophagy-lysosome pathway. *Acta*
264 *Neuropathol Commun* 4, 51 (2016).
- 265 21 Amick, J., Roczniak-Ferguson, A. & Ferguson, S. M. C9orf72 binds SMCR8,
266 localizes to lysosomes, and regulates mTORC1 signaling. *Mol Biol Cell* 27,
267 3040-3051 (2016).
- 268 22 Ugolino, J. *et al.* Loss of C9orf72 Enhances Autophagic Activity via
269 Deregulated mTOR and TFEB Signaling. *PLoS Genet* 12, e1006443 (2016).
- 270 23 Yang, M. *et al.* A C9ORF72/SMCR8-containing complex regulates ULK1 and
271 plays a dual role in autophagy. *Sci Adv* 2, e1601167 (2016).
- 272 24 Jung, J. *et al.* Multiplex image-based autophagy RNAi screening identifies
273 SMCR8 as ULK1 kinase activity and gene expression regulator. *Elife* 6
274 (2017).
- 275 25 Amick, J., Tharkeshwar, A. K., Amaya, C. & Ferguson, S. M. WDR41
276 supports lysosomal response to changes in amino acid availability. *Mol Biol*
277 *Cell* 29, 2213-2227 (2018).
- 278 26 Amick, J., Tharkeshwar, A. K., Talaia, G. & Ferguson, S. M. PQLC2 signals
279 lysosomal cationic amino acid abundance to the C9orf72 complex. *BioRxiv*
280 doi.org/10.1101/670034 (2019).
- 281 27 Farg, M. A. *et al.* C9ORF72, implicated in amyotrophic lateral sclerosis and
282 frontotemporal dementia, regulates endosomal trafficking. *Hum Mol Genet* 23,
283 3579-3595 (2014).
- 284 28 Webster, C. P. *et al.* The C9orf72 protein interacts with Rab1a and the ULK1
285 complex to regulate initiation of autophagy. *EMBO J.* 35, 1656-1676 (2016).
- 286 29 Lan, Y., Sullivan, P. M. & Hu, F. SMCR8 negatively regulates AKT and
287 MTORC1 signaling to modulate lysosome biogenesis and tissue homeostasis.
288 *Autophagy* 15, 871-885 (2019).
- 289 30 Shen, K. *et al.* Architecture of the human GATOR1 and GATOR1-Rag
290 GTPases complexes. *Nature* 556, 64-69 (2018).
- 291 31 Lawrence, R. E. *et al.* Structural mechanism of a Rag GTPase activation
292 checkpoint by the lysosomal folliculin complex. *Science* (2019).
- 293 32 Shen, K. *et al.* Cryo-EM Structure of the Human FLCN-FNIP2-Rag-Ragulator

294 Complex. *Cell* (2019).
295 33 Bar-Peled, L. *et al.* A Tumor Suppressor Complex with GAP Activity for the
296 Rag GTPases That Signal Amino Acid Sufficiency to mTORC1. *Science* 340,
297 1100-1106 (2013).
298 34 Tsun, Z. Y. *et al.* The Folliculin Tumor Suppressor Is a GAP for the RagC/D
299 GTPases That Signal Amino Acid Levels to mTORC1. *Mol. Cell* 52, 495-505
300 (2013).
301 35 Shen, K., Valenstein, M. L., Gu, X. & Sabatini, D. M. Arg78 of Nprl2
302 catalyzes GATOR1-stimulated GTP hydrolysis by the Rag GTPases. *J Biol*
303 *Chem* (2019).
304 36 Sztul, E. *et al.* ARF GTPases and their GEFs and GAPs: concepts and
305 challenges. *Mol Biol Cell* 30, 1249-1271 (2019).
306 37 Corrionero, A. & Horvitz, H. R. A C9orf72 ALS/FTD Ortholog Acts in
307 Endolysosomal Degradation and Lysosomal Homeostasis. *Curr Biol* 28,
308 1522-1535 e1525 (2018).
309 38 Jewell, J. L. *et al.* Metabolism. Differential regulation of mTORC1 by leucine
310 and glutamine. *Science* 347, 194-198 (2015).
311
312
313
314
315



316

317

318 **Fig.1: Cryo-EM structure of L-SCARF complex.**

319 **a**, Schematic diagram of the domain structure of L-SCARF complex. **b**, Cryo-EM
 320 density map (localfilter map, b-factor -50 \AA^2) and **c**, the refined coordinates of the
 321 complex shown as pipes and planks for α -helices and β -sheets, respectively. The
 322 domains color-coded as follows: SMCR8^{longin}, cornflower blue; SMCR8^{DENN}, dodger
 323 blue; C9orf72^{longin}, olive; C9orf72^{DENN}, goldenrod ; WDR41, medium purple.
 324 Organizations of **d**, SMCR8^{longin}: C9orf72^{longin} and **e**, SMCR8^{DENN}: C9orf72^{DENN}
 325 arrangement.

326

327

328

329

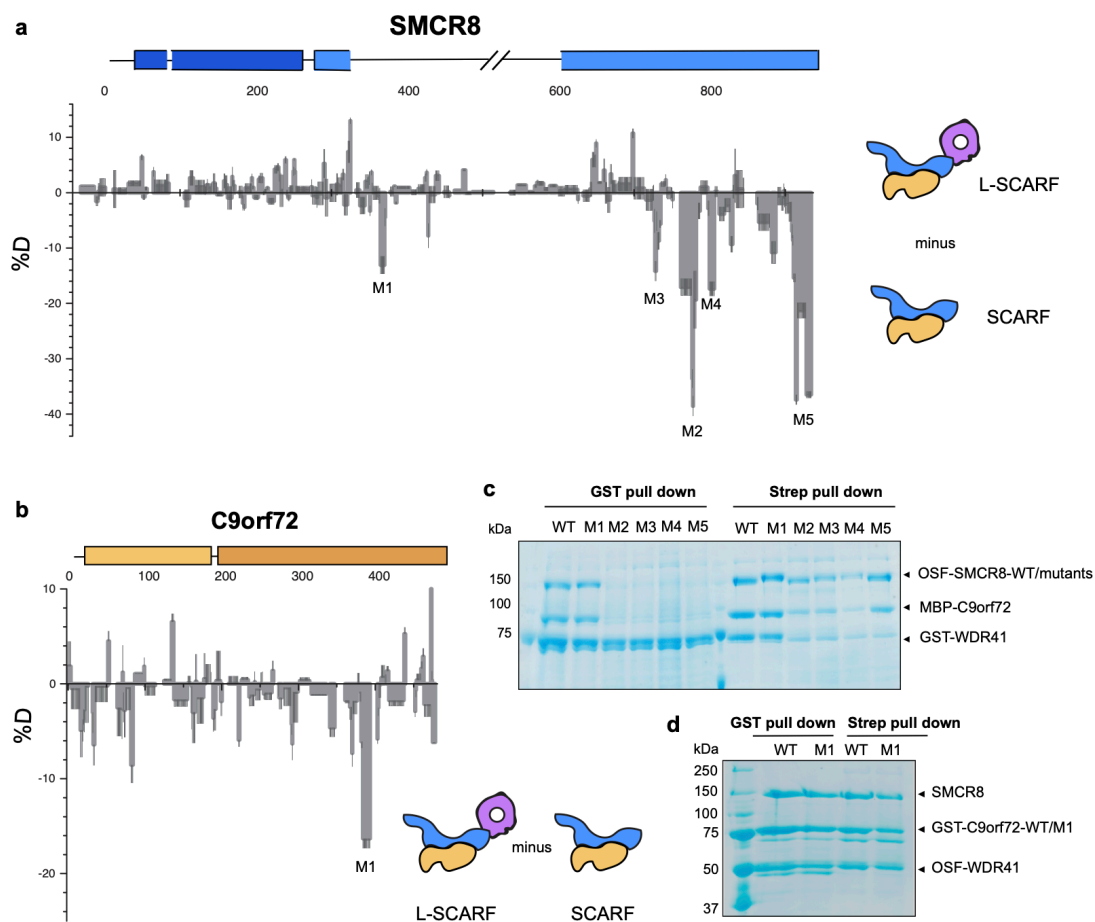
330

331

332

333

334



335

336

337 **Fig. 2: HDX-MS of SCARF in the absence of WDR41.**

338 **a**, Difference plot of percentage of deuterium incorporation of SMCR8 in heterotrimer
 339 versus dimer at 5 sec timepoint. **b**, Difference plot of percentage of deuterium
 340 incorporation of C9orf72 in heterotrimer versus dimer at 0.5 sec timepoint. **c**, Pull
 341 down experiment of SMCR8 mutants with wild type C9orf72 and WDR41. **d**, Pull
 342 down experiments of C9orf72 mutant with wild type SMCR8 and WDR41.

343

344

345

346

347

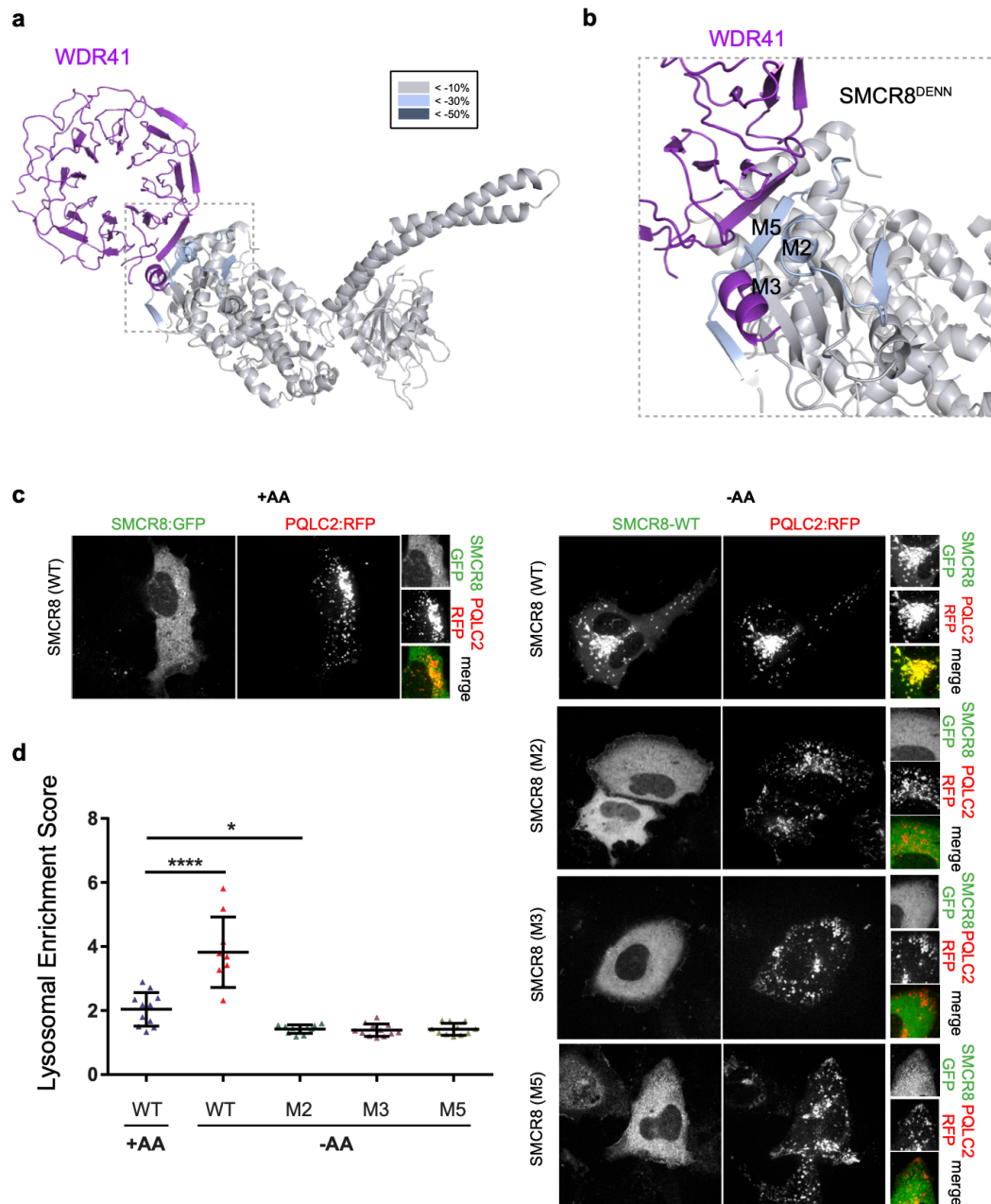
348

349

350

351

352



353

354

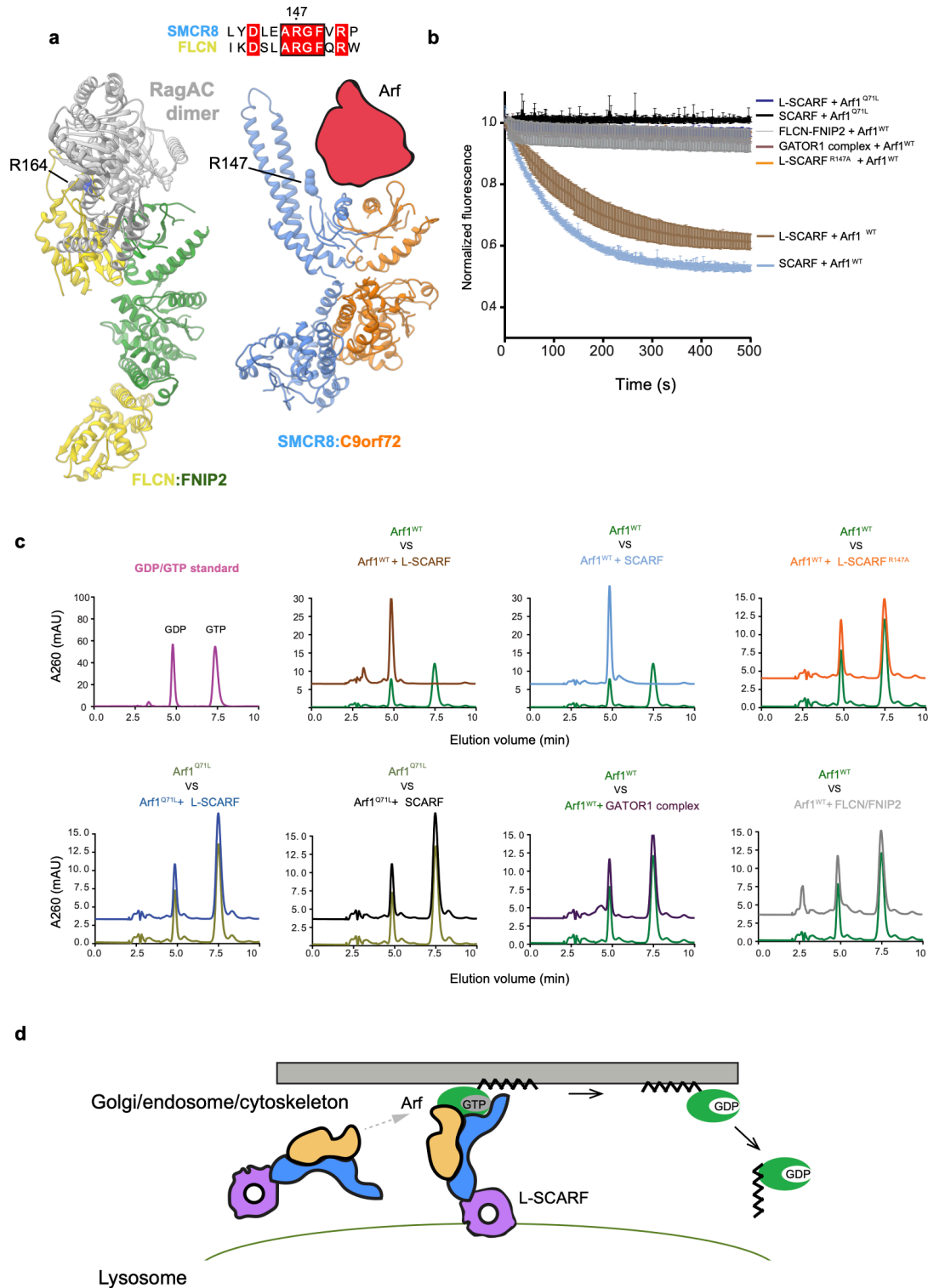
355 **Fig. 3: SMCR8 mutants fail to localize on lysosome.**

356 **a**, HDX uptake difference at 0.5 sec was mapped on SCARF. **b**, Close view of
 357 SMCR8-WDR41 interface, highlighting the SMCR8 mutants. **c**, SMCR8-PQLC2
 358 lysosome colocalization experiment in cells expressing the indicated SMCR8
 359 constructs under the indicated nutrient conditions. **d**, Quantification of SMCR8
 360 lysosomal enrichment score for immunofluorescence images in **c**. More than 10
 361 cells were quantified for each condition.

362

363

364



365

366

367 **Fig. 4: SCARF is a GAP for Arf proteins.**

368 **a**, Structure comparison of FNIP2-FLCN and SCARF, implying a potential binding
 369 site for substrates. The conserved Arg residue was shown in spherical representation.

370 **b**, Tryptophan fluorescence GTPase signal was measured for Arf1^{WT} or Q71L before and
 371 after addition of SCARF^{WT} or R147A -WDR41, SCARF, FLCN-FNIP2 or GATOR1

372 complex. **c**, HPLC-based GTPase assay with Arf1^{WT or Q71L} proteins in the absence
373 and addition of GAP complex as indicated. **d**, Model for Arf protein family activation
374 by SCARF-WDR41.
375
376

377 **Methods**

378

379 **Protein expression and purification**

380 Synthetic genes encoding SMCR8 were amplified by PCR and cloned into the
381 pCAG vector coding for an N-terminal twin-STREP-FLAG tag using KpnI and XhoI
382 restriction sites. The pCAG vector encoding an N-terminal GST followed by a TEV
383 restriction site or uncleaved MBP tag was used for expression of C9orf72. WDR41
384 was cloned into pCAG vector without a tag or with a GST tag for pull down
385 experiments. For the mutations of SMCR8 identified from HDX experiments,
386 SMCR8^{M1} (K363-L371) was mutated to MSDYDIPTTE, which is a 10-residue linker
387 derived from the pETM11 vector. SMCR8^{M2} (P771-Q778) or (K762-L782) for
388 lysosome localization experiments was mutated to GGKGS GGS. SMCR8^{M3}
389 (S729-V735) and SMCR8^{M4} (T807-D811) were made by mutating these regions to
390 GGKGS GG and GGKGS, respectively. SMCR8^{M5} was made by truncation after
391 residue 910K. C9orf72^{M1} (K388-L393) was mutated to polyAla. The SMCR8
392 arginine finger mutation R147A was made using two step PCR and cloned into the
393 expression vector.

394 HEK293-GnTi cells adapted for suspension were grown in Freestyle media
395 supplemented with 1% FBS and 1% antibiotic-antimycotic at 37 °C, 80 % humidity, 5
396 % CO₂, and shaking at 140 rpm. Once the cultures reached 1.5–2 million cells
397 mL⁻¹ in the desired volume, they were transfected as followed. For a 1 L transfection,
398 3 mL PEI (1 mg ml⁻¹, pH 7.4, Polysciences) was added to 50 mL hybridoma media
399 (Invitrogen) and 1 mg of total DNA (isolated from transformed E. coli XL10-gold) in
400 another 50 mL hybridoma media. 1 mg of transfection DNA contained equal mass
401 ratio of C9orf72 complex expression plasmids. PEI was added to the DNA, mixed and
402 incubated for 15 min at room temperature. 100 mL of the transfection mix was then
403 added to each 1 L culture. Cells were harvested after 3 days.

404 Cells were lysed by gentle rocking in lysis buffer containing 50 mM HEPES, pH
405 7.4, 200 mM NaCl, 2 mM MgCl₂, 1% (vol/vol) Triton X-100, 0.5 mM TCEP,
406 protease inhibitors (AEBSF, Leupeptin and Benzamidine) and supplemented with
407 phosphatase inhibitors (50 mM NaF and 10 mM beta-glycerophosphate) at 4 °C.
408 Lysates were clarified by centrifugation (15,000 g for 40 min at 4 °C) and incubated
409 with 5 mL glutathione Sepharose 4B (GE Healthcare) for 1.5 hr at 4 °C with gentle
410 shaking. The glutathione Sepharose 4B matrix was applied to a gravity column,
411 washed with 100 mL wash buffer (20 mM HEPES, pH 7.4, 200 mM NaCl, 2 mM
412 MgCl₂, and 0.5 mM TCEP), and purified complexes were eluted with 40 mL wash
413 buffer containing 50 mM reduced glutathione. Eluted complexes were treated with
414 TEV protease at 4 °C overnight. TEV-treated complexes were purified to

415 homogeneity by injection on Superose 6 10/300 (GE Healthcare) column that was
416 pre-equilibrated in gel filtration buffer (20 mM HEPES, pH 7.4, 200 mM NaCl, 2 mM
417 MgCl₂, and 0.5 mM TCEP). For long-term storage, fractions from the gel filtration
418 chromatography were frozen using liquid nitrogen and kept at -80 °C. SCARF and
419 L-SCARF were expressed and purified using the same protocol.

420 For expression of His₆-tagged Arf1 (residue E17-K181), Arf1 Q71L, Arf5
421 (residue Q17-Q180), Arf6 (residue R15-S175), Arf6 Q67L, His₆-Rab1a, His₆-Arl8a
422 (E20-S186) and His₆-Arl8b (E20-S186) proteins, plasmids were transformed into
423 *E.coli* BL21 DE3 star cells and induced with 0.5 mM IPTG at 18° C overnight. The
424 cells were lysed in 50 mM Tris-HCl pH 8.0, 300 mM NaCl, 2 mM MgCl₂, 5 mM
425 imidazole, 0.5 mM TCEP and 1 mM PMSF by ultrasonication. The lysate was
426 centrifuged at 15,000 g for 30 min. The supernatant was loaded into Ni-NTA resin
427 and washed with 20 mM imidazole and eluted with 300 mM imidazole. The eluate
428 was further purified on a Superdex 75 10/300 (GE Healthcare) column equilibrated in
429 20 mM HEPES, pH 7.4, 200 mM NaCl, 2 mM MgCl₂, and 0.5 mM TCEP. Rag,
430 FLCN-FNIP2 and GATOR1 complex were purified as described previously³¹.
431 GST-tagged Rab7 was expressed in the same conditions as above and purified with
432 GST resin, eluted in 50 mM reduced glutathione and applied on Superdex 200
433 column.

434

435 **Hydrogen/Deuterium exchange experiment**

436 Sample quality was assessed by SDS-PAGE before each experiment. Amide
437 hydrogen exchange mass spectrometry was initiated by a 20-fold dilution of 10 μM
438 L-SCARF or SCARF into 95 μl D₂O buffer containing 20 mM HEPES pH (pD 8.0),
439 200 mM NaCl, 1 mM TCEP at 30° C. Incubations in deuterated buffer were
440 performed at intervals from 0.5, 5, 50, 500 and 50,000 sec (0.5 sec was carried out
441 by incubating proteins with ice cold D₂O for 5 sec). All exchange reactions were
442 carried out in triplicate or quadruplicate. Backbone amide exchange was quenched at
443 0° C by the addition of ice-cold quench buffer (400 mM KH₂PO₄/H₃PO₄, pH 2.2).
444 The 50,000 sec sample served as the maximally labeled control. Quenched samples
445 were injected onto a chilled HPLC setup with in-line peptic digestion and then eluted
446 onto a BioBasic 5 μM KAPPA Capillary HPLC column (Thermo Fisher Scientific),
447 equilibrated in buffer A (0.05 % TFA), using 10-90 % gradient of buffer B (0.05 %
448 TFA, 90 % acetonitrile) over 30 mins. Desalted peptides were eluted and directly
449 analyzed by an Orbitrap Discovery mass spectrometer (Thermo Fisher Scientific).
450 The spray voltage was 3.4 kV and the capillary voltage was 37 V. The HPLC system
451 was extensively cleaned between samples. Initial peptide identification was
452 performed via tandem MS/MS experiments. A Proteome Discoverer 2.1 (Thermo

453 Fisher Scientific) search was used for peptide identification and coverage analysis
454 against entire complex components, with precursor mass tolerance ± 10 ppm and
455 fragment mass tolerance of ± 0.6 Da. Mass analysis of the peptide centroids was
456 performed using HDExaminer (Sierra Analytics), followed by manual verification of
457 each peptide.

458

459 **Cryo-EM grid preparation and data acquisition**

460 The purified L-SCARF complex was diluted to 0.8 μM in 20 mM HEPES pH
461 7.4, 2 mM MgCl_2 , and 0.5 mM TCEP and applied to glow-discharged C-flat (1.2/1.3,
462 Au 300 mesh) grids. The sample was vitrified after blotting for 2 sec using a Vitrobot
463 Mark IV (FEI) with 42 sec incubation, blot force 8 and 100 % humidity. The complex
464 was visualized with a Titan Krios electron microscope (FEI) operating at 300 kV with
465 a Gatan Quantum energy filter (operated at 20 eV slit width) using a K2 summit direct
466 electron detector (Gatan, Inc.) in super-resolution counting mode, corresponding to a
467 pixel size of 0.5745 \AA on the specimen level. In total, 3,508 movies were collected in
468 nanoprobe mode using Volta phase plate (VPP) with defocus collected around -60 nm.
469 Movies consisted of 49 frames, with a total dose of 59.8 $\text{e}^-/\text{\AA}^2$, a total exposure time
470 of 9.8 sec, and a dose rate of 8.1 $\text{e}^-/\text{pixel}/\text{sec}$. Data were acquired with SerialEM using
471 custom macros for automated single particle data acquisition. Imaging parameters for
472 the data set are summarized in Extended Data Table 1.

473

474 **Cryo-EM data processing**

475 Preprocessing was performed during data collection within Focus³⁹. Drift,
476 beam induced motion and dose weighting were corrected with MotionCor2⁴⁰ using 5
477 x 5 patches. CTF fitting and phase shift estimation were performed using Gctf v1.06
478 ⁴¹, which yielded the characterized pattern of phase shift accumulation over time for
479 each position. The data were manually inspected and micrographs with excess
480 ice-contamination or shooting on the carbon were removed. A total of 4,810,184
481 particles from 3,220 micrographs were picked using gautomatch
482 (<http://www.mrc-lmb.cam.ac.uk/kzhang/Gautomatch/>) and extracted with binning 4.
483 All subsequent classification and reconstruction steps were performed using
484 Relion3-beta⁴² or cryoSPARC v2⁴³. The particles were subjected to 3D classification
485 (K=5) using a 60 \AA low-pass filtered *ab initio* reference generated in cryoSPARC.
486 Around 2.2 million particles from the two best classes were selected for 3D
487 auto-refinement and another round of 3D classification (K=8, T=8, E-step=8) without
488 alignment. Some 1.8 millions particles from the best 6 classes were reextracted with
489 binning 2 and refined to 4.9 \AA , and further subjected to 2D classification without
490 alignment for removing contamination and junk particles. After another round of 3D

491 classification (K=4) with alignment, the best class was extracted and imported into
492 cryoSPARC v2 for another round of 2D classification. The cleaned up 571,002
493 particles were applied to CTF refinement, Bayesian polishing and further particles at
494 edges were removed in Relion 3. Final 381, 450 particles resulted in final resolution
495 of 3.8 Å with a measured map B-factor of -102 \AA^2 . More extensive 3D classification,
496 focus classification in Relion3 did not improve the quality of the reconstruction. Local
497 filtering and B-factor sharpening were done in cryoSPARC v2. All reported
498 resolutions are based on the gold-standard FSC 0.143 criterion.

499

500 **Atomic model building and refinement**

501 The model of WDR41 was generated with I-Tasser⁴⁴ and used 5nnz, 2ymu,
502 5wlc, 4nsx and 6g6m as starting models. The model of the C9orf72^{longin} domain was
503 generated based on the Nprl2^{longin} domain (pdb 6ces) in Modeller⁴⁵. The model of
504 SMCR8^{DENN} domain was generated from Modeller and RaptorX⁴⁶ using the
505 FLCN^{DENN} domain (pdb 3v42) or the *DENND1B*^{DENN} domain (pdb 3tw8) as
506 templates. The SMCR8^{longin} and C9orf72^{DENN} domain were generated with Phyre2⁴⁷
507 using FLCN^{longin} and FNIP2^{DENN} domain (pdb 6nzd) as templates. Secondary
508 structure predictions of each protein were carried out with Phyre2⁴⁷ or Psipred⁴⁸. The
509 models were docked into the 3D map as rigid bodies in UCSF Chimera⁴⁹. The
510 coordinates of the structures were manually adjusted and rebuilt in Coot⁵⁰. The
511 resulting models were refined using Phenix.real_space.refine in the Phenix suite with
512 secondary structure restraints and a weight of 0.1^{51,52}. Model quality was assessed
513 using MolProbity⁵³ and the map-vs-model FSC (Extended Data Table 1 and Extended
514 Data Fig. 4a). Data used in the refinement excluded spatial frequencies beyond 4.2 Å
515 to avoid over fitting. A half-map cross-validation test showed no indication of
516 overfitting (Extended Data Fig. 4b). Figures were prepared using UCSF Chimera⁴⁹
517 and PyMOL v1.7.2.1. The cryo-EM density map has been deposited in the Electron
518 Microscopy Data Bank under accession code EMD-21048 and the coordinates have
519 been deposited in the Protein Data Bank under accession number 6V4U.

520

521 **Live cell imaging**

522 800,000 HEK 293A cells were plated onto fibronectin-coated glass-bottom
523 Mattek dishes and transfected with the indicated wild type GFP-SMCR8 or mutants,
524 C9orf72, WDR41 and PQLC2-mRFP constructs with transfection reagent
525 Xtremegene. 24 hrs later, cells were starved for amino acids for one hr (-AA) or
526 starved and restimulated with amino acids for 10 mins (+AA). Cells in the -AA
527 condition were transferred to imaging buffer (10 mM HEPES, pH7.4, 136 mM NaCl,
528 2.5 mM KCl, 2 mM CaCl₂, 1.2 mM MgCl₂) and cells in the +AA condition were

529 transferred to imaging buffer supplemented with amino acids, 5 mM glucose, and 1%
530 dialyzed FBS (+AA) and imaged by spinning-disk confocal microscopy. Lysosomal
531 enrichment was scored as described³¹ using a home-built Matlab script to determine
532 the lysosomal enrichment of GFP SMCR8. The score was analyzed for at least ten
533 cells for each condition. Unpaired t-tests were calculated using Prism 6 (Graphpad).

534

535 **HPLC analysis of nucleotides**

536 The nucleotides bound to small GTPases were assessed by heating the protein
537 to 95 °C for 5 min followed by 5 min centrifugation at 16,000 g. The supernatant was
538 loaded onto a HPLC column (Eclipse XDB-C18, Agilent). Nucleotides were eluted
539 with HPLC buffer (10 mM tetra-n-butylammonium bromide, 100 mM potassium
540 phosphate pH 6.5, 7.5 % acetonitrile). The identity of the nucleotides was compared
541 to GDP and GTP standards.

542

543 **HPLC-based GAP assay**

544 HPLC-based GTPase assays were carried out by incubating 30 µl of GTPases
545 (30 µM) with or without GAP complex at a 1:50 molar ratio for 30 min at 37 °C.
546 Samples were boiled for 5 min at 95 °C and centrifuged for 5 min at 16,000 g The
547 supernatant was injected onto an HPLC column as described above. The experiments
548 are carried out in triplicate and one representative plot is shown.

549

550 **Tryptophan fluorescence-based GAP assay**

551 Fluorimetry experiments were performed using a FluoroMax-4 (Horiba)
552 instrument and a quartz cuvette compatible with magnetic stirring, a pathlength of 10
553 mm, and were carried out in triplicate. The Trp fluorescence signal was collected
554 using 297 nm excitation (1.5 nm slit) and 340 nm emission (20 nm slit). Experiments
555 were performed in gel filtration buffer at room temperature with stirring. Data
556 collection commenced with an acquisition interval of 1 sec. 2 µM GTPase was added
557 to the cuvette initially. Once the signal was equilibrated, SCARF^{WT or R147A}-WDR41 or
558 SCARF, FLCN-FNIP2, or GATOR1 complex was pipetted into the cuvette at a 1: 10
559 molar ratio. Time t = 0 corresponds to GAP addition. The fluorescence signal upon
560 GAP addition was normalized to 1 for each experiment. Mean and standard error of
561 the mean of three replicates per conditions were plotted.

562

563

564

565

566

567 **Methods references:**

568

- 569 39 Biyani, N. *et al.* Focus: The interface between data collection and data
570 processing in cryo-EM. *J Struct Biol* 198, 124-133 (2017).
- 571 40 Zheng, S. Q. *et al.* MotionCor2: anisotropic correction of beam-induced
572 motion for improved cryo-electron microscopy. *Nat Methods* 14, 331-332
573 (2017).
- 574 41 Zhang, K. Gctf: Real-time CTF determination and correction. *J Struct Biol*
575 193, 1-12 (2016).
- 576 42 Zivanov, J. *et al.* New tools for automated high-resolution cryo-EM structure
577 determination in RELION-3. *Elife* 7 (2018).
- 578 43 Punjani, A., Rubinstein, J. L., Fleet, D. J. & Brubaker, M. A. cryoSPARC:
579 algorithms for rapid unsupervised cryo-EM structure determination. *Nat*
580 *Methods* 14, 290-296 (2017).
- 581 44 Zhang, Y. I-TASSER server for protein 3D structure prediction. *BMC*
582 *Bioinformatics* 9, 40 (2008).
- 583 45 Webb, B. & Sali, A. Protein structure modeling with MODELLER. *Methods*
584 *Mol Biol* 1137, 1-15 (2014).
- 585 46 Peng, J. & Xu, J. RaptorX: exploiting structure information for protein
586 alignment by statistical inference. *Proteins* 79 Suppl 10, 161-171 (2011).
- 587 47 Kelley, L. A., Mezulis, S., Yates, C. M., Wass, M. N. & Sternberg, M. J. The
588 Phyre2 web portal for protein modeling, prediction and analysis. *Nat Protoc*
589 10, 845-858 (2015).
- 590 48 McGuffin, L. J., Bryson, K. & Jones, D. T. The PSIPRED protein structure
591 prediction server. *Bioinformatics* 16, 404-405 (2000).
- 592 49 Pettersen, E. F. *et al.* UCSF Chimera--a visualization system for exploratory
593 research and analysis. *J Comput Chem* 25, 1605-1612 (2004).
- 594 50 Emsley, P. & Cowtan, K. Coot: model-building tools for molecular graphics.
595 *Acta crystallographica. Section D, Biological crystallography* 60, 2126-2132
596 (2004).
- 597 51 Afonine, P. V. *et al.* Real-space refinement in PHENIX for cryo-EM and
598 crystallography. *Acta Crystallogr D Struct Biol* 74, 531-544 (2018).
- 599 52 Adams, P. D. *et al.* PHENIX: a comprehensive Python-based system for
600 macromolecular structure solution. *Acta crystallographica. Section D,*
601 *Biological crystallography* 66, 213-221 (2010).
- 602 53 Chen, V. B. *et al.* MolProbity: all-atom structure validation for
603 macromolecular crystallography. *Acta crystallographica. Section D,*
604 *Biological crystallography* 66, 12-21 (2010).

605

606 **Acknowledgments:**

607 We thank D. Toso, S. Fromm, K. L. Morris, V. Kasinath and P. Tobias for cryo-EM
608 advice and support, X. Shi for HDX support, S. Fromm for comments on the
609 manuscript, C. Behrends and G. Stjepanovic for suggestions and contributions to the
610 early stages of the project, and R. Lawrence for cell imaging advice. Access to the
611 FEI Titan Krios was provided through the BACEM UCB facility. This work was
612 supported by NIH grants R01GM111730 (J.H.H.) and R01GM130995 (R.Z.), the
613 Bakar Fellows program (J.H.H.), the Pew-Stewart Scholarship for Cancer Research
614 and Damon Runyon-Rachleff Innovation Award (R.Z.), and a postdoctoral fellowship
615 from the Association for Frontotemporal Degeneration (M.-Y.S.).

616

617 **Author contributions:**

618 Conceptualization, M.-Y.S. and J.H.H.; Investigation, M.-Y.S. and R. Z.; Supervision,
619 J.H.H., R.Z.; Writing- original draft, M.-Y.S. and J.H.H.; Writing- review and editing,
620 all authors.

621

622 **Corresponding author:**

623 Correspondence to James H. Hurley: jimhurley@berkeley.edu

624

625

626 **Competing interests**

627 J.H.H. is a scientific founder and receives research funding from Casma Therapeutics.
628 R.Z. is co-founder and stockholder in Frontier Medicines Corp.

629

630 **Data availability**

631 EM density map has been deposited in the EMDB with accession number
632 EMD-21048. Atomic coordinates for the L-SCARF have been deposited in the PDB
633 with accession number 6V4U.

634

635

636

637

638

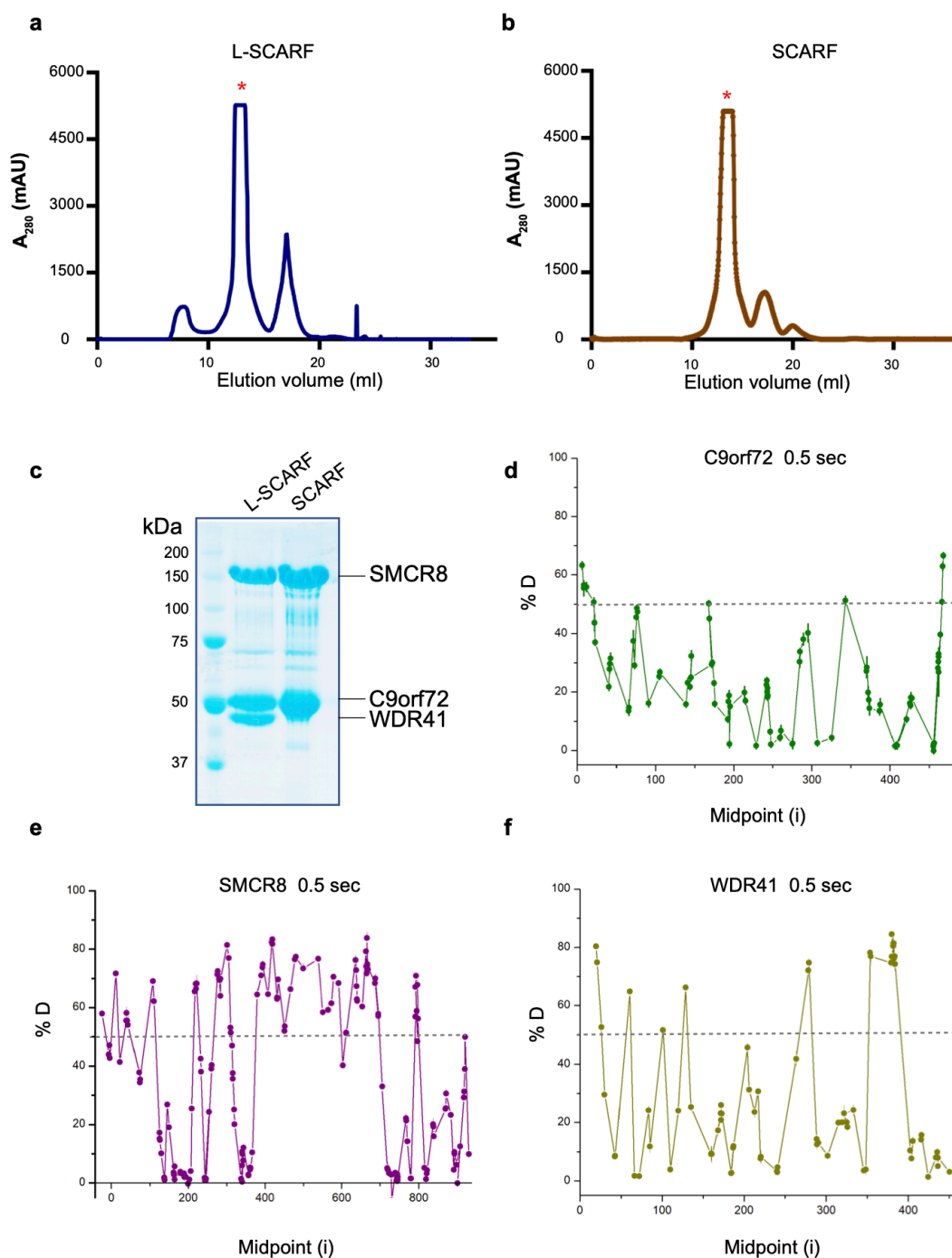
639

640

641

642

643 **Extended data figures/table**



645 **Extended Data Fig.1: Purification of the L-SCARF and SCARF complex as well**
646 **as the HDX data for trimer.**

647 **a**, The superose 6 gel filtration elution profile for L-SCARF complex. **b**, The superose
648 6 gel filtration elution profile for SCARF complex. mAU, milli-absorbance units. **c**,
649 The purified full length L-SCARF and SCARF were analyzed by SDS-PAGE. **d-f**,
650 Deuterium uptake data for L-SCARF complex at 0.5 sec timepoint with error bars
651 from triplicate measurements. Peptides with more than 50 % deuterium uptake are the

652 flexible regions. Y axis represents the average percent deuteration. X axis
653 demonstrates the midpoint of a single peptic peptide.

654

655

656

657

658

659

660

661

662

663

664

665

666

667

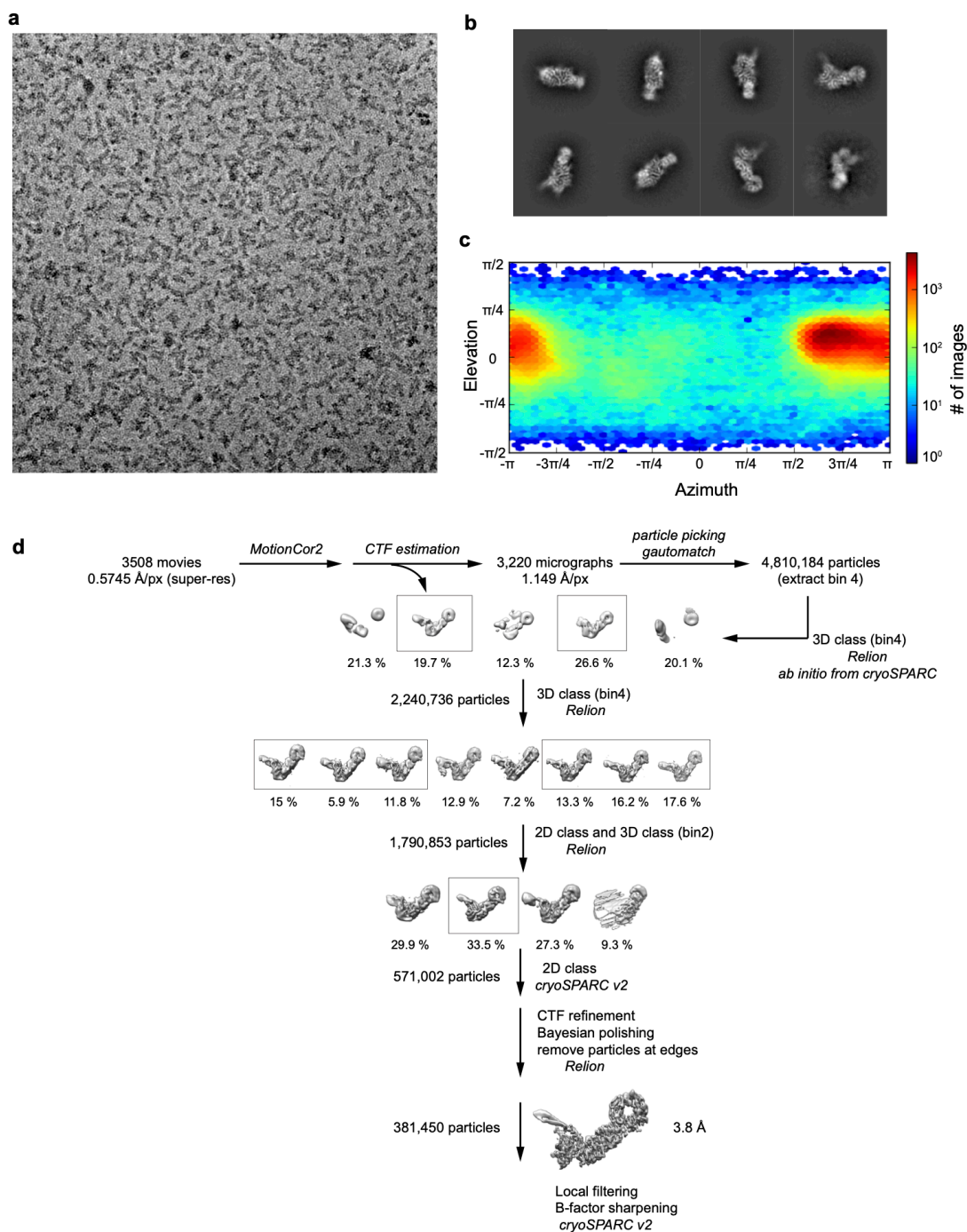
668

669

670

671

672



673

674 **Extended Data Fig. 2: Cryo-EM data processing.**

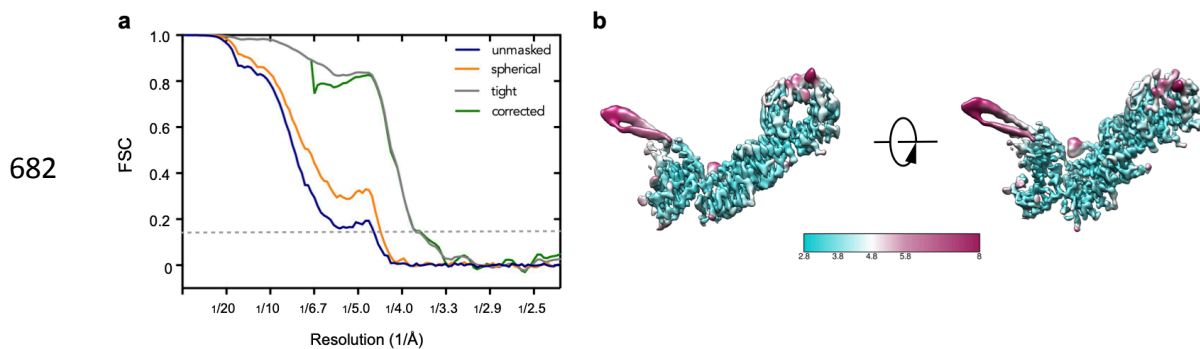
675 **a**, Representative cryo-EM micrograph of L-SCARF complex. **b**, Representative 2D
676 classes. **c**, Orientation distribution of the aligned particles. **d**, Image processing
677 procedure.

678

679

680

681



683 **Extended Data Fig.3: Resolution estimation of the cryo-EM map. a**, Comparison
684 between FSC curves. **b**, L-SCARF complex map color-coded by the local resolution
685 estimation.

686

687

688

689

690

691

692

693

694

695

696

697

698

699

700

701

702

703

704

705

706

707

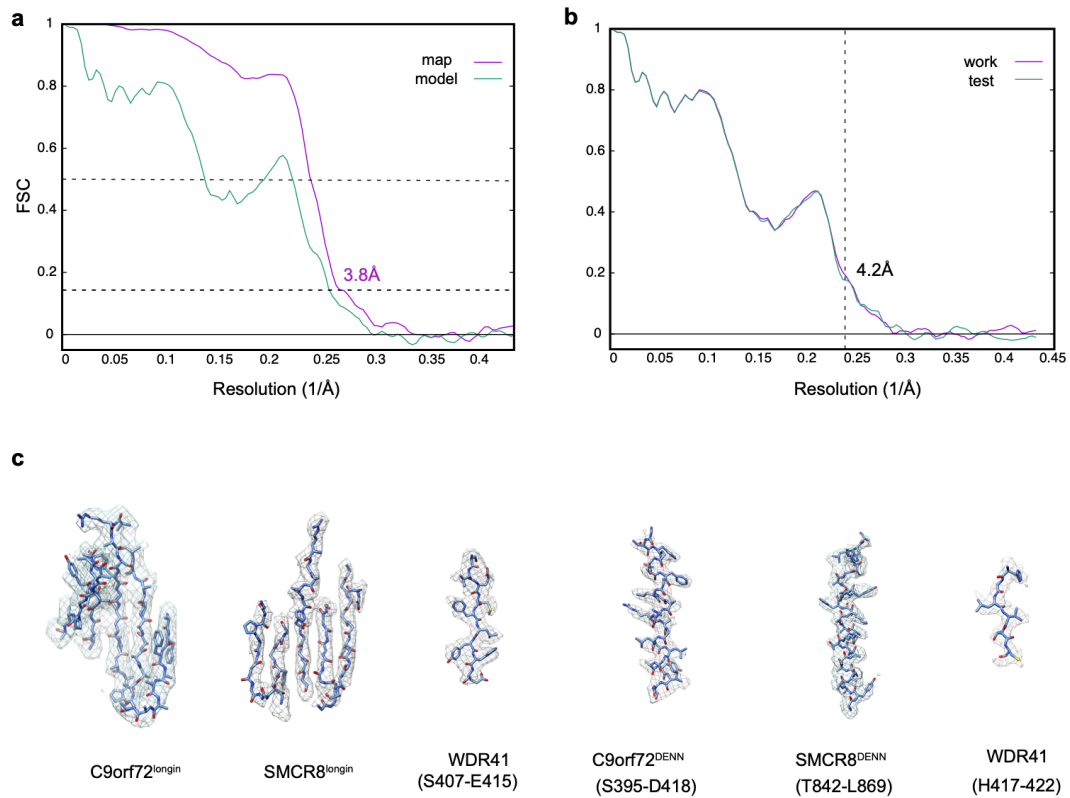
708

709

710

711

712



713

714

715 **Extended Data Fig. 4: Model building and validation.**

716 **a**, Refinement and map-vs-model FSC. **b**, Cross-validation test FSC curves to assess

717 overfitting. The refinement target resolution (4.2 Å) is indicated. **c**, Refined

718 coordinate model fit of the indicated region in the cryo-EM density.

719

720

721

722

723

724

725

726

727

728

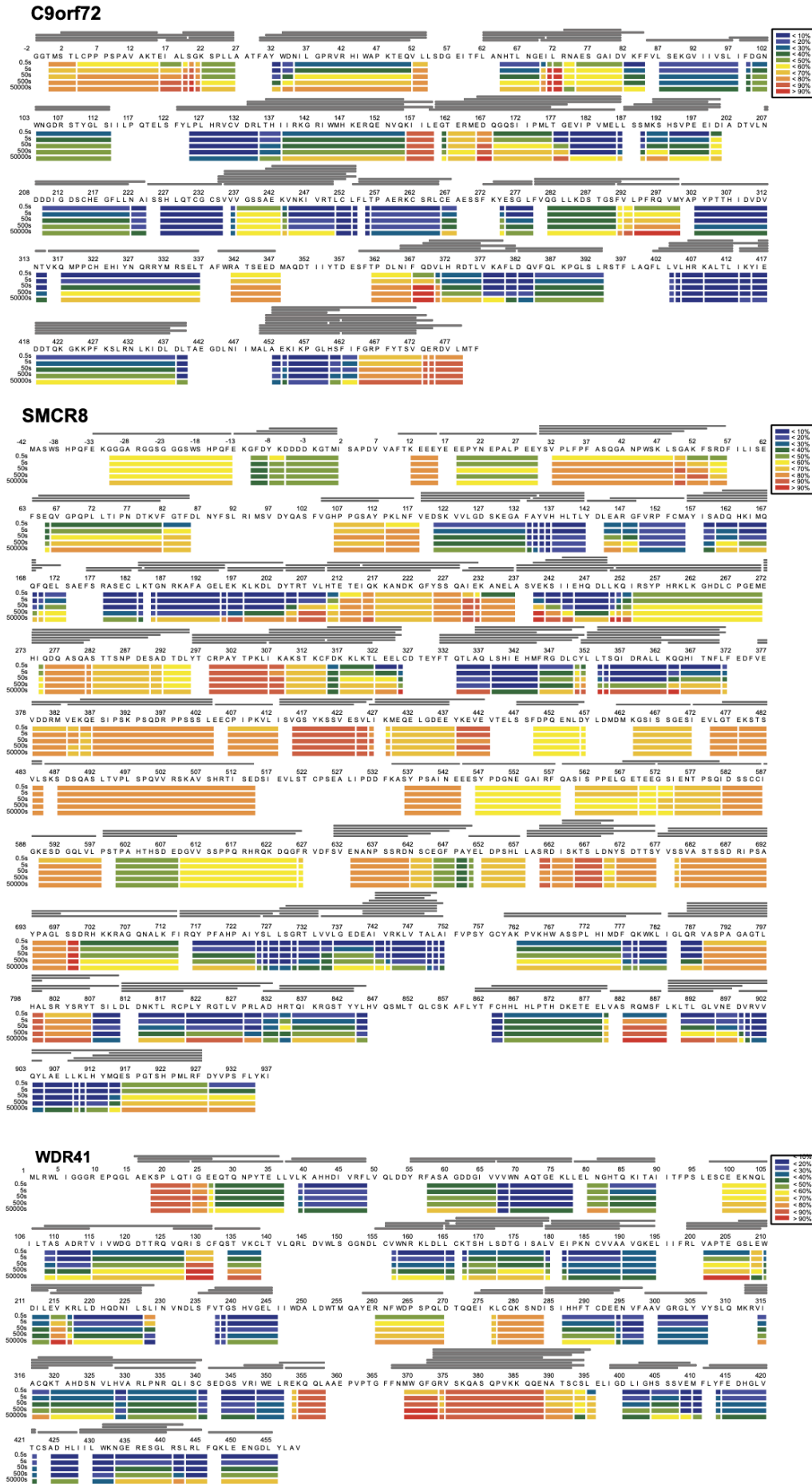
729

730

731

732

733



735 **Extended Data Fig. 5: Deuterium uptake of L-SCARF complex.**

736 HDX- MS data are shown in heatmap format where peptides were represented using
737 rectangular strips above the protein sequence. Absolute deuterium uptake after 0.5 , 5 ,
738 50 , 500 and 50,000 sec were indicated by a color gradient below the protein
739 sequence.

740

741

742

743

744

745

746

747

748

749

750

751

752

753

754

755

756

757

758

759

760

761

762

763

764

765

766

767

768

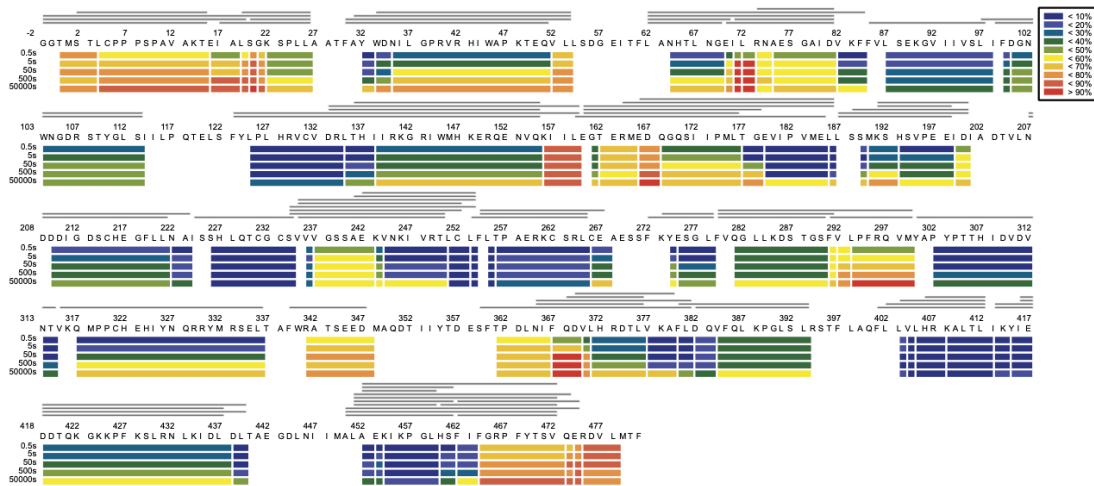
769

770

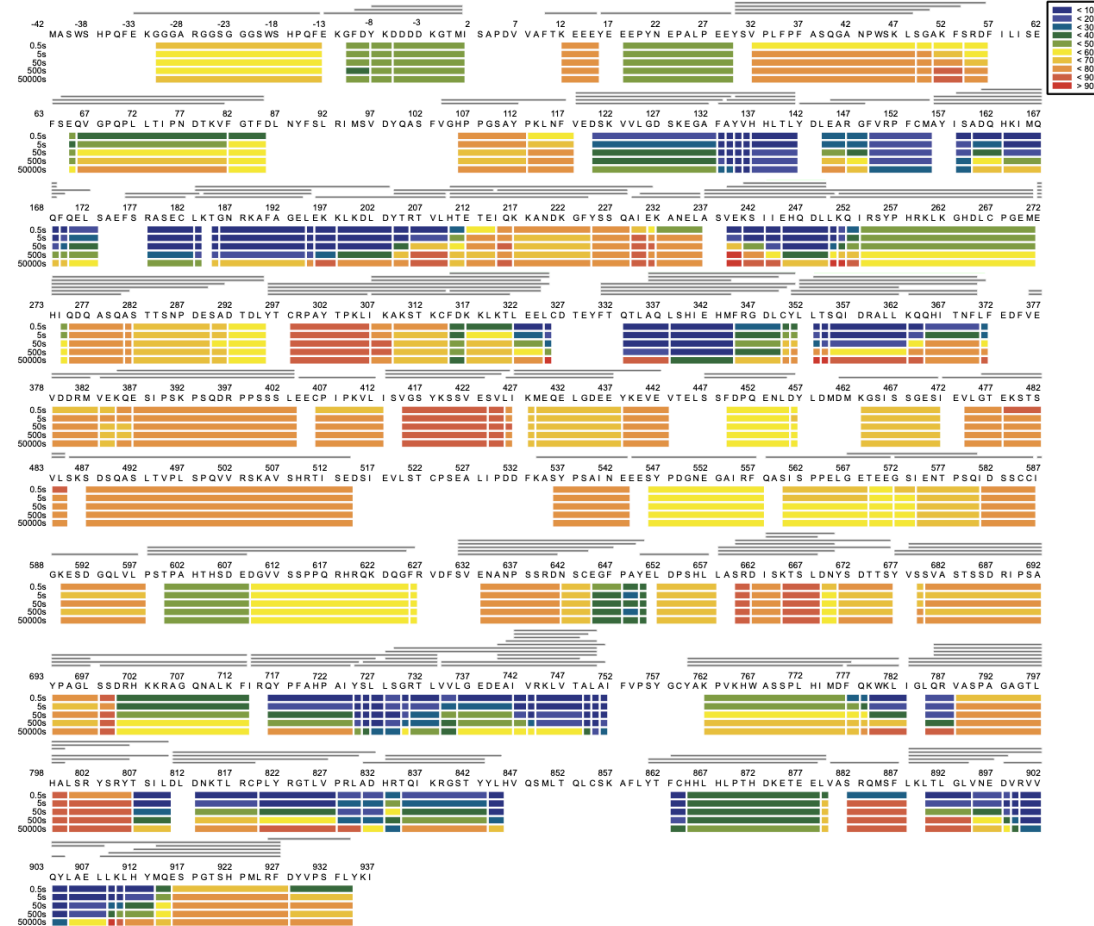
771

772

C9orf72



SMCR8



773

774

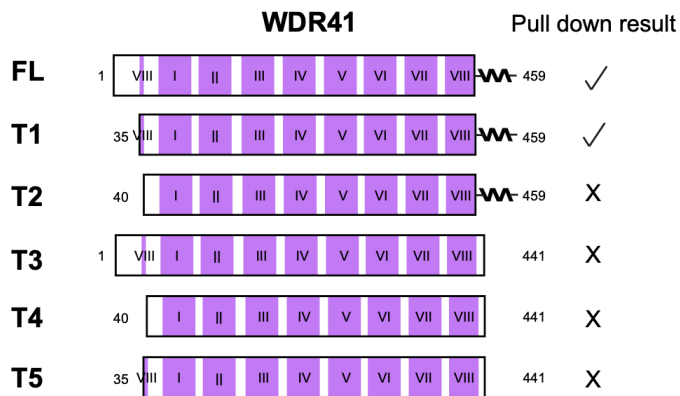
775 **Extended Data Fig.6: Deuterium uptake of SCARF complex.**

776

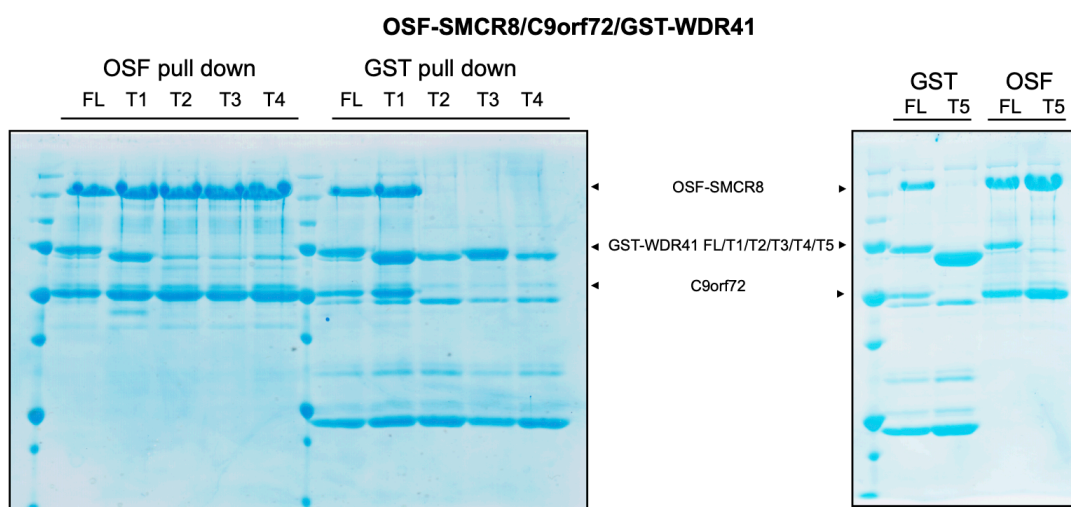
777

778

779



780



781 **Extended Data Fig. 7: Pull down experiment of WDR41 mutants with SCARF**
 782 **complex.**

783

784

785

786

787

788

789

790

791

792

793

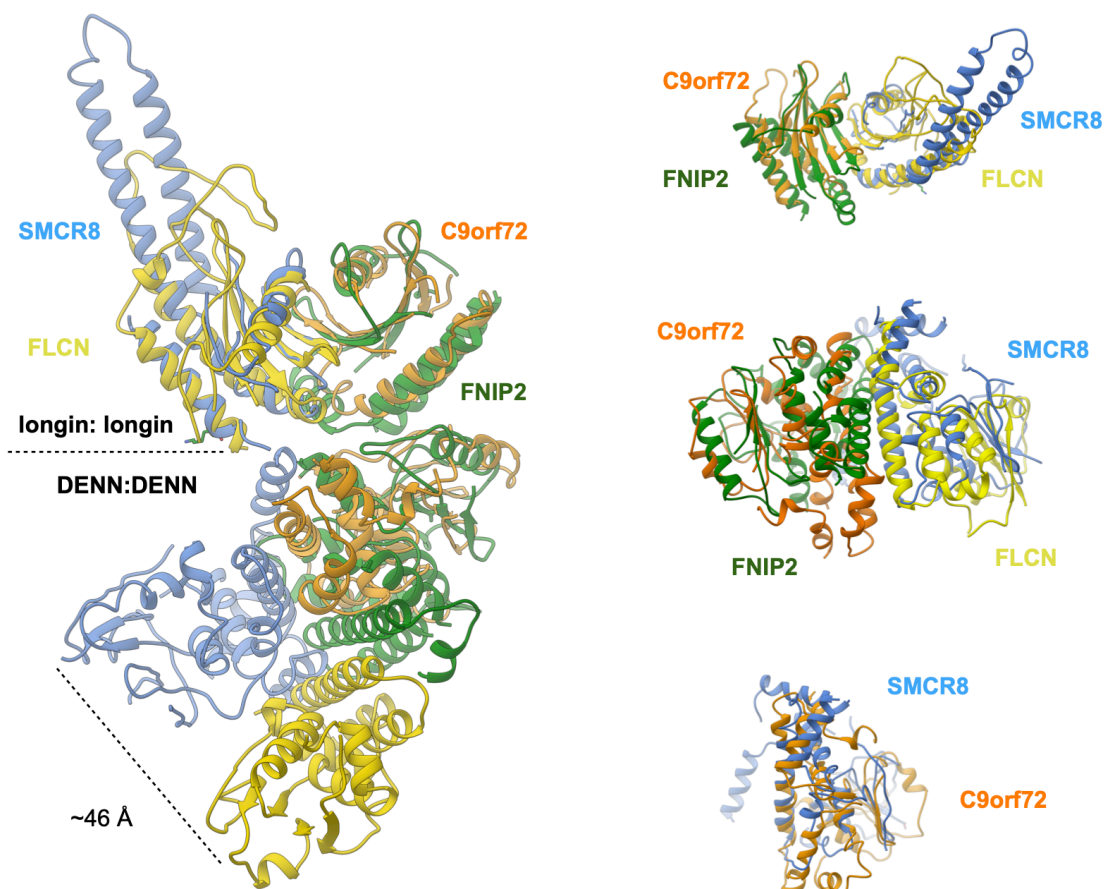
794

795

796

797

798



799

800 **Extended Data Fig. 8: Structural comparison between SCARF and**
801 **FNIP2-FLCN.**

802

803

804

805

806

807

808

809

810

811

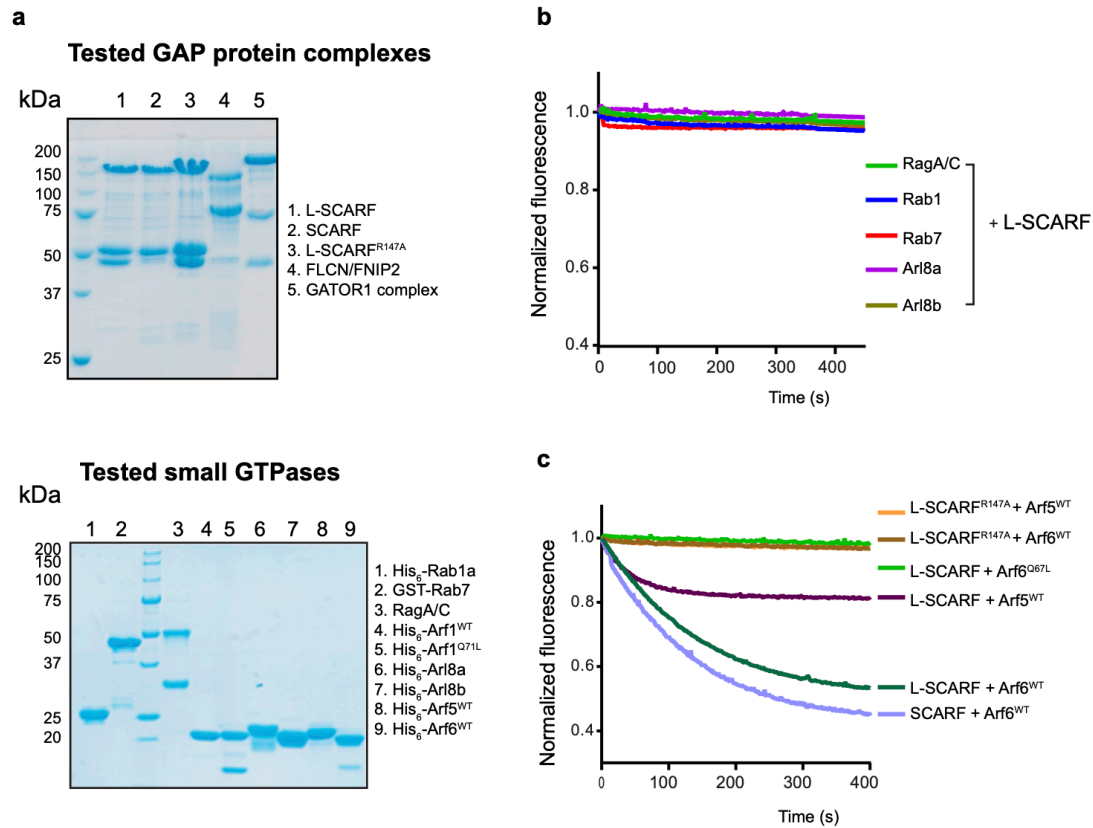
812

813

814

815

816



817

818 **Extended Data Fig. 9: GTPase assay for different small GTPases with L-SCARF**
 819 **complex.**

820 **a**, SDS-PAGE of GAP protein complex (top) and GTPase proteins (bottom) used in
 821 the experiments. **b**, Tryptophan fluorescence GTPase signal was measured for
 822 purified Rag, Arl8a, Arl8b, Rab1a and Rab7 before and after addition of L-SCARF. **c**,
 823 Tryptophan fluorescence GTPase signal was measured for purified Arf6^{WT} or Q67L or
 824 Arf5^{WT} and before and after addition of SCARF^{WT} or R147A-WDR41 or SCARF^{WT}.

825

826

827

828

829

830

831

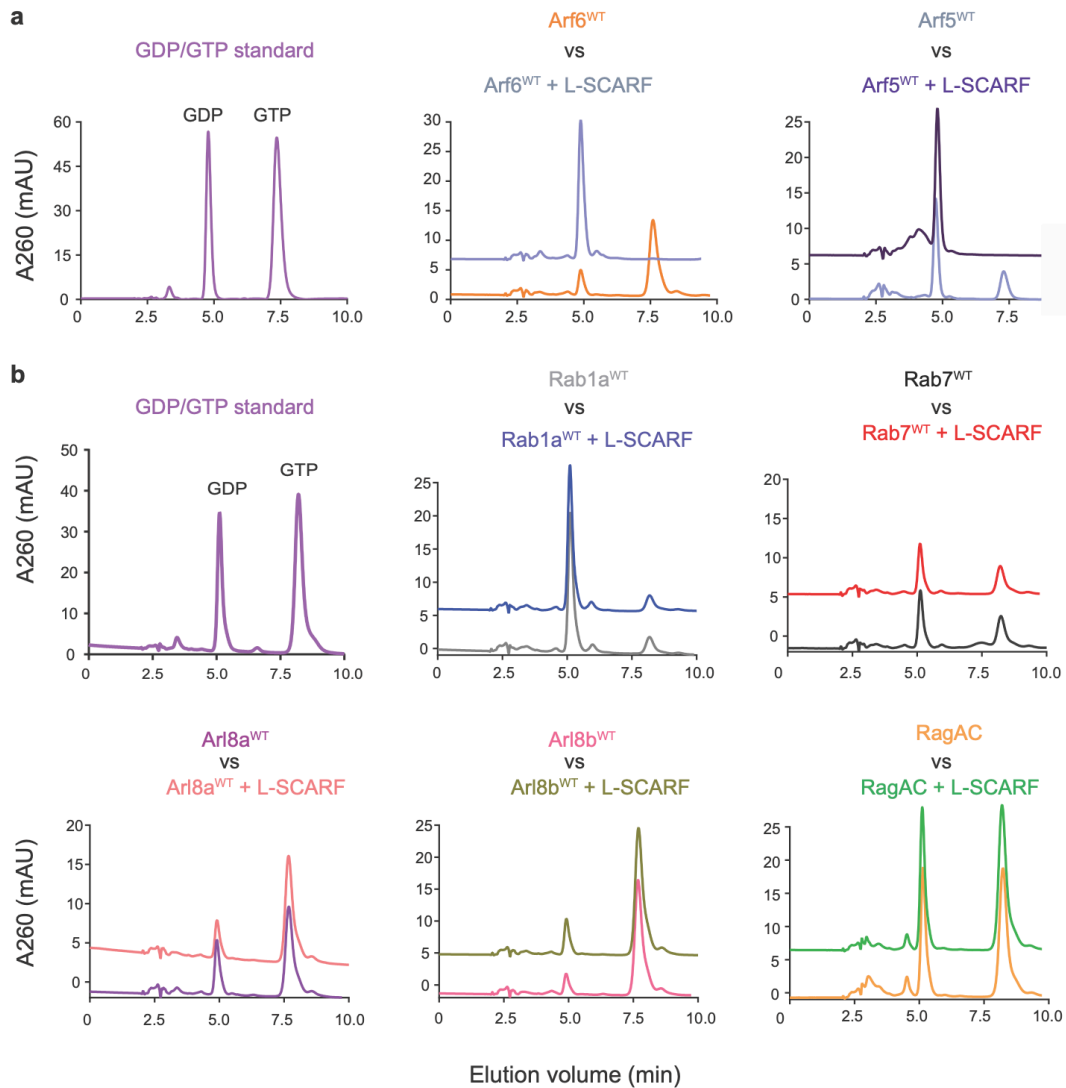
832

833

834

835

836



837

838 **Extended Data Fig.10: HPLC-based GTPase assay with Arf6, Arf5, Rab1a, Rab7,**
839 **Arl8a, Arl8b and RagA/C proteins in the absence and addition of L-SCARF**
840 **complex as indicated.**

841

842

843

844

845

846

847

848

849

850

851

852 **Extended Data Table 1. Cryo-EM data collection, refinement and validation**
 853 **statistics**

	L-SCARF (EMDB-21048) (PDB 6V4U)
Data collection and processing	
Microscope	Titan Krios
Magnification (calibrated)	43,516
Camera	Quantum-K2 Summit
Voltage (kV)	300
Electron exposure (e ⁻ /Å ²)	59.6
Volta phase plate	Yes
Pixel size (Å)	1.149
Symmetry imposed	C1
Initial particle images (no.)	4,810,184
Final particle images (no.)	381,450
Map resolution (Å)	3.80
FSC threshold	0.143
Refinement	
Initial model used (PDB code)	-
Map sharpening <i>B</i> factor (Å ²)	-50
Model composition	
Non-hydrogen atoms	6817
Protein residues	1119
Ligands	0
R.m.s. deviations	
Bond lengths (Å)	0.002
Bond angles (°)	0.443
Validation	
MolProbity score	1.75
Clashscore	6.07
Poor rotamers (%)	0
Ramachandran plot	
Favored (%)	93.79
Allowed (%)	6.21
Disallowed (%)	0.00

854

855

856

857

858

Extended Data Dataset S1. HDX Data Summary (L-SCARF and SCARF)		
Data Set	L-SCARF	SCARF
# of Peptides	SMCR8: 178	SMCR8: 178
	C9orf72: 90	C9orf72: 90
	WDR41: 73	
Sequence coverage (%)	SMCR8: 88.8	SMCR8: 88.8
	C9orf72: 87	C9orf72: 87
	WDR41: 80.4	
Redundancy	SMCR8: 2.8	SMCR8: 2.9
	C9orf72: 3.1	C9orf72: 3.2
	WDR41: 2.1	
Average standard deviation (%)	SMCR8: 0.84	SMCR8: 0.98
	C9orf72: 0.88	C9orf72: 0.91
	WDR41: 0.85	
Deuterium time course analyzed (sec)	0.5/5/50/500/50,000	0.5/5/50/500/50,000
Control samples (sec)	50,000	50,000
Replicates	Triplicates/Quadruplicate	Triplicates/Quadruplicate
Back-exchange (mean)	SMCR8: 32.23	SMCR8: 31.03
	C9orf72: 42.46	C9orf72: 42.69
	WDR41: 37.20	

859

860

861

862

863

864 **References**

865

866

867